The 3-5 MHz global reflectivity map of Mars by MARSIS/Mars Express: implications for the current inventory of subsurface HO

J. Mouginot, A. Pommerol, W. Kofman, P. Beck, B. Schmitt, A. Herique, C. Grima, A. Safaeinili, J.J. Plaut

HAL Id: hal-00693814

https://hal.archives-ouvertes.fr/hal-00693814

Submitted on 3 May 2012

Accepted Manuscript

The 3-5 MHz global reflectivity map of Mars by MARSIS/Mars Express: implications for the current inventory of subsurface H_2O

J. Mouginot, A. Pommerol, W. Kofman, P. Beck, B. Schmitt, A. Herique, C. Grima, A. Safaeinili, J.J. Plaut

Please cite this article as: Mouginot, J., Pommerol, A., Kofman, W., Beck, P., Schmitt, B., Herique, A., Grima, C., Safaeinili, A., Plaut, J.J., The 3-5 MHz global reflectivity map of Mars by MARSIS/Mars Express: implications for the current inventory of subsurface H_2O, *Icarus* (2010), doi: 10.1016/j.icarus.2010.07.003
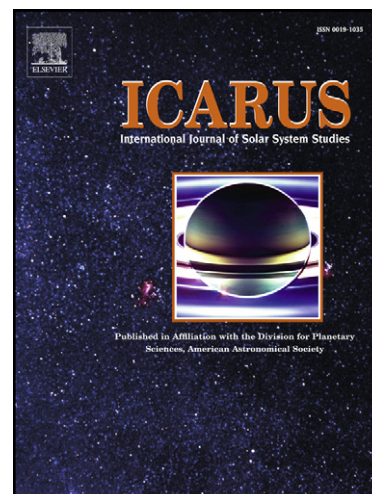
1 **The 3-5 MHz global reflectivity map of Mars by**

2 **MARSIS/Mars Express: implications for the current**

3 **inventory of subsurface H$_2$O.**

4

5 J. Mouginot[1,2], A. Pommerol[1,3], W. Kofman[1], P. Beck[1], B. Schmitt[1], A. Herique[1], C.

6 Grima[1], A. Safaeinili[4] and J.J. Plaut[4]

7

8 [1]Laboratoire de Planétologie de Grenoble, UJF-Grenoble I/CNRS, France.

9 [2]University of California Irvine, CA, USA.

10 [3]Physikalisches Institut, Universitaet Bern, Switzerland.

11 [4]Jet Propulsion Laboratory, Pasadena, CA, USA.

12

13

18

19 **Abstract**

20

21   We extracted the surface echo power from two years of MARSIS

22   measurements. The retrieved values are calibrated to compensate for changes in the

23   distance of the spacecraft to the surface and for the attenuation of the signal by the

24   ionosphere. The results are used to build the first global map of surface echo power at

25   3-5 MHz. The surface echo power variations are primarily caused by km-scale surface

26   roughness. Then, we derive the values of dielectric constant of the shallow subsurface

27   materials by normalizing the surface echo power map using a simulation of MARSIS

28   signal from the MOLA topography. As a result, we obtain a map that characterizes the

29   dielectric properties of the materials down to a few decameters below the surface.

30   Dielectric properties vary with latitude, with high values in mid-latitudes belts (20-

31   40°) and lower values at both equatorial and high latitudes. From the comparison of

32   MARSIS reflectivity map to GRS observations, we conclude that the reflectivity

33   decrease observed poleward of 50-60° corresponds to the onset of water-ice

34   occurrence within the regolith. Assuming homogenous ground composition and

35   texture at the scale of the MARSIS resolution cell, our inferred volume of ground

36   water ice is of 10^6 km^3, equivalent to a polar cap. Low reflectivity areas are also

37   observed in equatorial regions. From radar studies alone, equatorial low dielectric

38   constant values could have different interpretations but the correlation with GRS

39   hydrogen distribution rather points toward a water related explanation.

40

1. Introduction

The Martian surface has been scrutinized for decades by a variety of imaging and spectroscopic techniques, sensitive to the properties of the first micrometers to millimeters of the surface. Meanwhile, subsurface investigations remained limited to indirect studies until the arrival of the Mars Odyssey mission in 2001. Data from the Gamma Ray Spectrometer (GRS) were used to map the average chemical composition of the first meter below the surface (e.g. Boynton et al., 2007). The spatial distribution of hydrogen (inferred to be present in the form of ground ice) in both hemispheres is one of the major results of this instrument (Boyton et al., 2002; Feldman et al., 2002; Mitrofanov et al., 2002). In order to infer and map the properties of the Martian regolith and crust below this depth of 1 m, "ground penetrating" geophysical techniques are required.

Whereas low frequency radar has been used in the past to probe the subsurface of Mars using terrestrial ground based instruments, the Mars Advanced Radar for Subsurface and Ionospheric Sounding instrument (MARSIS) on board Mars Express (Picardi et al. 2005) was the first radar sounder to operate from an orbiting probe around Mars. It has then been joined by the Shallow Subsurface Radar (SHARAD) on board Mars Reconnaissance Orbiter (Seu et al., 2007). MARSIS is a decameter radar sounder that operates in 1 MHz-wide frequency bands centered at 1.8, 3, 4 and 5 MHz, whereas SHARAD operates at higher frequency (20 MHz) and with a larger bandwidth (10 MHz), which leads to smaller penetration depth but higher vertical resolution. These two instruments measure 2D "radargrams" that represent cross-sections of the Martian subsurface displaying discrete or continuous reflections of the radar waves at interfaces between materials of different dielectric constant (e.g. Plaut

65   et al. 2007; Watters et al., 2007; Grima et al. 2009). Penetration depth of MARSIS can

66   reach 4 kilometers in clear water ice (Plaut et al. 2007), and this instrument was able

67   to map the bedrock/ice interface below Mars polar caps.

68   Here, instead of looking at individual radargrams, we build a global map of

69   Mars by extracting the surface echo power from each frame (pulse) of each

70   radargram. This so-called "reflectivity map" gives important information on the

71   composition and physical properties of the upper part of the Martian crust at a global

72   scale. Radar reflectivity maps of the Moon at different frequencies have already been

73   measured in the past from ground-based instruments and used to infer important

74   properties of the Lunar terrains (Evans 1962; Evans and Pettengill 1963). In

75   particular, Campbell and Hawke, 2005 show that reflectivity values measured at the

76   wavelength: $\lambda = 70$ cm can be influenced by the composition of terrains buried more

77   than 50 m deep in some cases, demonstrating the ability of this method to probe at

78   large depth. In the case of Mars, some measurements had also been obtained using

79   ground based radio telescopes at $\lambda = 3.5$ to 70 cm (Simpson et al., 1992; Harmon et

80   al., 1999) or spacecraft as Mars-3 and Mars-4 spacecraft (Krupenio et al. 1977) and

81   Viking orbiter 2 at $\lambda = 13.1$ cm (Simpson et al., 1979) but were rather limited in terms

82   of spatial resolution and / or geographic extent. The reflectivity values obtained from

83   these measurements have been used to estimate the dielectric constant of surface

84   materials (Pettengill et al., 1973; Downs et al., 1973, 1975; Simpson et al., 1982).

85   Spatial variability of the value of the dielectric constant has been interpreted in terms

86   of variations of bulk density (Krupenio et al. 1977) and/or compositional variations

87   (Campbell and Ulrich, 1969) of subsurface materials.

88   In this article, we present the method used to extract the surface echo power,

89   and the corrections required to build the global dielectric map from MARSIS

90   measurements. We show that the obtained map provides unique information on the

91   nature of the surface geological material, and more generally on Mars geology and

92   climatology.

93

94 **2. Methods**

95

96 **2.1. Extraction of the surface echoes**

97

98   In a first step, the surface echo power values are extracted from the data.

99 MARSIS radargrams are composed of about a thousand frames, with each frame

100 corresponding to a vertical sounding of the Martian surface (figure 1). Radar echoes

101 appear when the transmitted waves meet abrupt changes in dielectric constant. The

102 first echo in the radargram corresponds mostly to the surface echo, because lateral

103 echoes (so called clutter) and subsurface echoes arrive later due to a longer distance

104 between reflectors and spacecraft. Furthermore, the intensity of the surface echo is

105 generally much higher than that of clutter or subsurface echoes. Using these

106 characteristics, we assume that the first echo returned corresponds to surface

107 reflection and we define a selection criteria C to localize the surface echo expressed

108 as:

109 $$C(i) = \frac{|S(i)|^2}{\mathrm{mean}(|S(i-1:i-30)|^2)} \qquad (1)$$

110 where S is the MARSIS signal in a given frame (512 samples) and i is the temporal

111 index inside the frame. Equation 1 computes the contrast between a bin and the signal

112 average over the 30-bin window preceding it.

113   C is maximum when $|S(i)|^2$ is maximum and $\mathrm{mean}(|S(i-1:i-30)|^2)$, equal to

114 the power level of the noise galactic and thermal), is minimum. This condition is only

115 satisfied for the surface echo, i.e. the only echo that can precede the surface echo is a

116 noise. An example of detection is given in figure 2 for orbit 2787. Once the surface

117   signal has been identified, the amplitude of the surface echo can easily be extracted as

118   shown on figure 1.

119   We have systematically applied this process to the MARSIS data, between

120   orbit 2300 and orbit 5200. Respectively about 0.6, 1.3 and 0.8 millions of

121   measurements were extracted from the frequency bands centered at 3, 4 and 5 MHz.

122   Band 1, centered at 1.8 MHz, is not used in this study because the number of

123   measurements was too small.

124

125   **2.2. Estimation of surface echo power**

126

127   The surface echo power largely depends on the attenuation of the

128   electromagnetic waves between the spacecraft and the surface, which is mainly due to

129   range attenuation and ionospheric absorption. In the following sections, we describe

130   the method used to correct these effects.

131

132   **2.2.1. Range attenuation**

133

134   Intensity of the surface echoes can be estimated by using a simplified radar

135   equation applying Snell's law for a vertically incident electromagnetic wave on a flat

136   surface. When we assume altitude of the satellite as R, the peak power of surface echo

137   can be estimated as:

138    $$P_r = \frac{P_t G^2 \lambda^2}{4(4\pi R)^2} r_{0,1} \quad (2)$$

139   where P_t, G, λ and $r_{0,1}$ are the peak power of transmitted RF pulses, the antenna

140   gain, the wavelength and the reflectivity of the surface, respectively. Thus, the

141   intensity of a surface echo is mainly dependent on the propagation range R, the

142   observation wavelength $\lambda = 2\pi c / \omega$ and antenna gain G (G=1.64 for a matched dipole

143   antenna condition).

144   The received power decreases with R^2 (equation 2). The Mars Express orbit is

145   elliptical and the spacecraft altitude during MARSIS passes varies between about 250

146   and 1000 km. It is therefore necessary to compensate for the power losses due to

147   altitude change, and we simply normalize the surface echo power by the squared

148   altitude of the spacecraft.

149

150   **2.2.2. Ionospheric absorption**

151

152   As described by Safaeinili et al. (2003), the plasma layer (ionosphere)

153   attenuates the MARSIS radar waves. The attenuation of electromagnetic waves per

154   meter of ionospheric plasma is given by:

155    $$A = 4.61 \times 10^{-5} \frac{n_e(z) \nu(z)}{\omega^2 + \nu(z)^2} \qquad (3)$$

156   where n_e is the electron density (m^{-3}) at altitude z (m), ν the electron collision

157   frequency (rad s^{-1}) and ω is the pulsation of the radar wave (radian frequency).

158   For MARSIS data, we have a two-way ionospheric propagation and the total

159   attenuation of the radar waves therefore becomes:

160    $$\int A dz = 2 \times 4.61 \times 10^{-5} \int \frac{n_e(z) \nu(z)}{\omega^2 + \nu(z)^2} dz \qquad (4)$$

161   The main parameters controlling absorption (equation 4) are the electron

162   density and collision frequency profiles that depend on the neutral density. As these

163   profiles are related to the ionization due to the solar EUV (extreme ultra violet)

164   radiation, the absorption changes on Mars have a first order dependence on solar

165   zenith angle. Safaeinili et al. (2003) have described in detail this phenomenon for

166   different states (day/night, etc…) of the Martian ionosphere.

167   An accurate estimation of absorption requires knowledge of the exact state of

168   the ionosphere and the neutral atmosphere (i.e. the density and collision profiles) for

169   each frame. These profiles are not measured and therefore we cannot precisely

170   calculate absorption. However, the correction of the dispersion effect (variation of

171   wave velocity with frequency) due to the ionosphere (Safaeinili et al. 2007, Mouginot

172   et al. 2008) provides a value of the total electron content (TEC) and, as TEC is the

173   integral of the electron density, this value is a good proxy to estimate absorption.

174   Figure 3a shows that the surface echo power on MARSIS data decreases as

175   TEC increases. In this figure, we used the entire set of signal measurements for the 4

176   MHz band. For a given value of TEC, the surface echo power varies over a 10dB

177   range due to the variable reflectivity of the different Martian terrains. This trend is

178   consistent with equation 4, which shows that electron density enhances absorption.

179   The signal decreases until a threshold is reached at about 30 dB below the

180   maximum power. This threshold corresponds to the MARSIS noise level. Table 1

181   summarizes, for each frequency band, the values of SZA (Solar Zenith Angle) or TEC

182   at which the signal becomes lost in the noise. We have chosen to remove the data

183   outside the limits defined in Table 1. Furthermore, we did not use observations that

184   show a very low signal power. In these cases, very high attenuation is probably due to

185   the increased electron density created by precipitation and radiation during solar flares

186   (Espley et al. 2007).

187   The next step consists in evaluating the behavior of the surface echo power as

188   a function of the TEC values. We compute the mean surface echo power for the

189   overall data set with a bin for TEC of $2x10^{13}$ electrons per square meter. The result is

190   presented in figure 3b. We use this curve of mean surface echo power as function of

191   TEC to normalize the data to compensate for absorption. The normalized data plotted

192   in figure 4 are constant on average as function of TEC.

193

194   **2.3 Surface echo power**

195

196   After extracting the surface echo power from the echo histories and correcting

197   them for range dependence and ionospheric absorption, we plot the global map of the

198   surface echo power in figure 5a. We averaged the data from multiple measurements

199   with a bin size of 0.5 degrees. MARSIS is a nadir-looking radar and the Mars Express

200   polar orbit does not allow us to sound the surface beyond about 87°N and 87°S. The

201   surface echo power values for the different frequency bands are very similar and have

202   thus been combined on this map to provide better coverage of the Martian surface.

203   However for local or regional studies, it could also be useful in the future to compare

204   the reflectivity measured in several frequency bands to study materials and/or

205   structures that could change the surface reflectivity as a function of frequency (e.g.,

206   Mouginot et al. 2008).

207   Several parameters might affect the surface echo power: surface roughness,

208   slope distribution and the dielectric constant of the surface materials. Most

209   backscattering models separate the effect of the dielectric constant (material

210 chemistry) from those of topography (roughness, slopes) (Ulaby et al. 1986; Picardi et

211 al. 2004). The reflectivity of the surface $r_{0,1}$ (equation 2) can be expressed by the

212 equation:

213 $r_{0,1} = \Gamma_s(\varepsilon) f_s(rms_s, \lambda)$ (5)

214 where Γ_s is the Fresnel reflectivity terms and f_s is the backscattering term (geometric

215 scattering). The function f_s is only dependent on the surface topography (i.e. the

216 roughness and the slopes).

217 The surface roughness at MARSIS wavelength is due to slight variations of

218 the surface heights over horizontal scale of the tens to hundred meters (figure 5c). The

219 slope distribution effect is due to surface altitude variation on a scale of a few hundred

220 to thousands meters. The surface echo is made from nadir return, which is a coherent

221 specular reflection of the emitted wave at the surface interface. This nadir echo is

222 mainly reflected on the first Fresnel zone, which has a diameter varying between 5

223 and 16 km (depending on the spacecraft altitude and emitted wavelength). The slope

224 distribution inside the first Fresnel zone results in a scattering of the signal to off-

225 nadir directions, which is related to a decrease of surface reflectivity.

226 As expected for a decametric radar waves, we observe in figure 5 that the

227 roughness at kilometer-scale (Kreslavsky and Head, 2000) is highly correlated to the

228 surface reflectivity due to slope distribution effect. The roughest terrains on Mars,

229 such as the Olympus Mons aureole, Valles Marineris, the Argyre crater rim display

230 very low surface echo power. Highlands Plateau, which is a heavily cratered region in

231 the southern hemisphere, presents globally a lower reflectivity compared to the

232 smoother northern plains (Vastistas Borealis). The smoothest terrains as the volcanic

233 plateau in Tharsis region or Amazonis Planitia are characterized by a very high

234 reflectivity.

235   Only few localized terrains that are smooth at kilometer-scale present low

236   reflectivity, such as the linear dune regions around the north polar cap (mostly in

237   Olympia Planitia), which are very rough at small scales and smoother at large scales

238   (Kreslavsky and Head, 2000). An image (figure 6) provided by the High Resolution

239   Imaging Science Experiment (HiRISE) on board Mars Reconnaissance Orbiter

240   (MRO) illustrates this small-scale roughness, showing dunes spaced in the range of

241   50-100 m, which corresponds exactly to the range of MARSIS wavelength. In this

242   particular case, the coherent part of the signal vanishes and only the incoherent part

243   (clutter) remains, as observed on the radargrams of orbit #3674 between frames 80

244   and 130 (figure 6). This region is typically an area where the roughness effect on the

245   signal is really strong compared to the effect of slope distribution.

246   However, only few regions are really rough at 10-100 meters scale and it

247   seems that the main effect on surface reflectivity is due to slope distribution

248   (kilometer-scale roughness). In addition, due to the lack of a global DEM at the

249   required spatial resolution, we cannot model the effect of small scale (< 100 m)

250   roughness. Thus, we have decided to neglect the effect of this roughness and to only

251   take into account the larger-scale slope distribution. Locally, this assumption could be

252   wrong (i.e. dune fields shown in figure 6). In such a case, we expect errors on the

253   retrieved reflectivity values up to 3 dB (Campbell and Shepard, 2003). However,

254   comparisons of the final dielectric map (figures 7 and 8) with the MOLA pulse width

255   map (Neumann et al., 2003), which describes roughness at 1-20 m and SHARAD

256   reflectivity map (unpublished data) which is sensitive to 1-15 m roughness do not

257   show any systematic correlation at global scale. Therefore, we do not think that

258   neglecting the < 100 roughness has any major effect for this global scale study.

259

260   **2.4 Simulation of MARSIS data**

261

262   In order to obtain maps showing the dielectric properties of surface materials,

263   we have to correct for the effects of relief on the signal and then calibrate the resulting

264   reflectivity. A method for simulating MARSIS echo histories due to local topography

265   has been developed to help in the interpretation of the observational data. For this

266   simulation, the surface is modeled using the facet method (Nouvel 2002; Nouvel et al.

267   2004), which is an extension of the Kirchhoff model. Such a model can be used

268   because of the low surface roughness at radar wavelengths and offers a significant

269   gain in calculation time. The synthetic faceted surface is generated from MOLA data

270   (Smith et al. 2001).

271   All MARSIS orbits have been simulated and we have extracted the surface

272   echo power in the same way as for actual MARSIS data. The dielectric constant of the

273   surface is kept constant in the simulation. Thus, the simulation makes possible the

274   estimation of the contribution of large-scale scattering resulting from slope

275   distribution. We can now consider the simulation as a reference for the surface echo

276   power in order to correct the roughness and topographic effects.

277   The result of all the simulations is shown in figure 5b as a global map of the

278   expected surface echo power of the Martian surface. Note that the Olympia Planitia

279   region is characterized by a high-simulated surface echo power compared to the real

280   power (see figure 5a). As the facet size in the simulation is about 460 m (due to the

281   limited MOLA resolution), the topography of the dunes is not captured by the digital

282   elevation model. This shows the limit of the simulation that is unable to simulate the

283   small-scale scattering resulting from surface roughness over a horizontal scale of tens

284   of meters or less.

285   The generation of a simulated map makes it possible to normalize the surface

286   echo power extracted from the MARSIS data. Finally we estimate the Fresnel

287   reflectivity $\Gamma_s(\varepsilon)$ by dividing the MARSIS data by the simulated data (see equation 5).

288   The result of this correction is shown in figure 7.

289   The Fresnel reflection coefficient $\Gamma_s(\varepsilon)$ at normal incidence at the plane interface

290   between two media with refractive indexes n_i and n_j respectively is defined as

291   followed:

292    $$\Gamma = \frac{n_i - n_j}{n_i + n_j} \quad (6)$$

293   The relation between the dielectric constant ε and refractive index n is $n = \sqrt{\varepsilon}$. The

294   reflectivity of an interface is given by $R = |\Gamma|^2$. For the surface interface, the equation

295   6 can be reduced to:

296    $$\Gamma = \frac{1 - n_j}{1 + n_j} \quad (7)$$

297   where n_j is the refractive index of the surface materials and n_i, the refractive index of

298   the atmosphere taken as 1.

299   Using equation 7, we easily convert $\Gamma_s(\varepsilon)$ into dielectric constant.

300   As the received power is still not calibrated in an absolute way, we use the regions of

301   the North and South Polar Layered Deposits (NPLD and SPLD) as a reference. We

302   adjusted the result in figure 7 by multiplying the whole map by a constant. This

303   constant is evaluated such that the estimated water ice reflectivity values in polar

304   layered deposit is matched (Plaut et al. 2007, Grima et al. 2009). We use: $\varepsilon' = 3.1$ and

305    $\Gamma = 0.275$. We can test the validity of this method by comparing our estimates of

306   dielectric constant to the values determined in the Ascraeus Mons region by Carter et

307   al. (2009). By analyzing SHARAD radar signal propagation between the surface and

308   shallow interfaces, they found values of permittivity ranging from 6.2 to 17.3 in the

309   Northern volcanic flows, with an average of 12.2, while in the southern volcanic flow,

310   values between 7.0 and 14.0 were estimated with an average of 9.8. In the same area,

311   the value we estimate for this area using surface power echo is of $11^{+11}_{-4} (n = 80)$. This

312   result is in fair agreement with Carter et al. (2009).

313

314 ## 3. Results and discussion

315

316 ### 3.1 Global geographic variations

317

318   Examination of the global dielectric map (figure 7) reveals significant spatial

319 variations over the planet. The most obvious feature is the latitude-dependent pattern

320 in reflectivity. The equatorial region displays generally low values, the mid-latitudes

321 generally high values, and the high latitudes generally low values again. The low-

322 reflectivity pattern in the equatorial regions is interrupted by very high reflectivity on

323 the Tharsis volcanic plateau, including Solis, Sinai and Daedalia plana, and the area

324 between the Tharsis Montes and Olympus Mons. In the mid-latitude bands, the largest

325 continuous patch of high reflectivity is on the northern side of the Elysium Mons

326 shield. The northern high latitudes are generally lower in reflectivity than the southern

327 high latitudes, with the exception of the area north of Alba Patera. The south residual

328 polar cap has a very low reflectivity due to interferences within the thin layer of CO_2

329 ice, causing much weaker surface reflections compared to reflections from a pure

330 water ice surface as described in details by Mouginot et al. 2009. Bands of apparent

331 low reflectivity in the Terra Cimmeria region are probably uncorrected artifacts

332 related to the interaction of the remnant crustal magnetics and the ionosphere

333 (Safaeinili et al. 2007, Mouginot et al. 2008).

334   Two main parameters are likely to control the dielectric constant of the layer

335 involved in the reflection process: the composition (chemistry, mineralogy, water

336 content and physical state) and the density of the constituent materials. Because water

337 ice presents a low dielectric constant (typically ~3.1) compared to igneous rocks (~8)

338 at MARSIS wavelengths, the presence of a significant amount of ice in the layer

339   involved in the reflection process will lead to a decrease in surface reflectivity,

340   compared to a dry, dense rock layer. However, low-density materials can also lead to

341   such low values of the effective dielectric constant and the use of complementary

342   datasets is crucial to build robust interpretations. We undertook systematic

343   comparisons between the MARSIS surface dielectric map, visible albedo maps,

344   topographic maps, the water concentration map derived from neutron spectroscopy,

345   and the thermal inertia map derived from TES (Thermal Emission Spectrometer on

346   Mars Global Surveyor) data.

347

348   **3.2 Latitudinal variations and the onset of ground-ice**

349

350   Examination of the MARSIS global map (figure 8a, b) and the corresponding

351   longitudinally averaged profile (figure 9) reveals a strong latitudinal dependence of

352   dielectric constant. For both hemispheres, the highest values (6 - 10) are observed at

353   tropical latitudes. These values are in agreement with laboratory measurements on dry

354   igneous rocks (Campbell and Ulrichs, 1969; Heggy et al., 2007) and are consistent

355   with igneous basaltic to granitic rocks. Variations of materials density are probably

356   responsible for the observed variability of the dielectric constant within igneous

357   terrains.

358   Poleward of around 50-60° in both hemispheres, terrains show a steep

359   decrease of dielectric constant down to values of 3 – 4. Climate related processes are

360   likely responsible for the observed latitudinal variations (Head et al., 2003), and the

361   comparison with other observations of the Martian surface strongly suggests that this

362   dielectric constant decrease corresponds to the onset of water-ice occurrence within

363   the regolith. For the current average water vapor atmospheric content, the frost point

364 at Mars surface is around 200 K. Average temperatures below the frost point are

365 reached for latitudes in excess of 30 to 45° in the Northern hemisphere and 40° in the

366 Southern hemisphere. Permanent stability of water ice is possible at depth, where the

367 sub-surface is insulated from the diurnal and seasonal temperature fluctuations. As

368 ice is not stable on the surface, we expect the ground ice to be overlaid by a layer of

369 dry regolith whose thickness depends on latitude, soil physical properties, and the

370 seasonal evolution of surface humidity (Mellon and Jakosky, 1991; Schorghofer and

371 Aharonson, 2005).

372   The MARSIS dielectric transition is not associated to a systematic change in

373 surface albedo or thermal inertia (figure 10), which implies that the surface

374 geological material does not change much upon crossing this transition. There is a

375 general agreement between the latitudinal distribution of near-surface (~top meter)

376 ground ice detected by GRS and the dielectric decrease observed by MARSIS

377 (figures 8 and 10). In the case of the southern hemisphere there is a good agreement

378 between the latitude of the ground-ice determined by MARSIS and GRS, with an

379 average latitude of 48-50°, almost constant with regard to longitude. This ground-ice

380 extent is also in good agreement with the calculated stability limit for the currently

381 observed atmospheric conditions (Mellon and Jakosky, 1991; Schorghofer and

382 Aharonson, 2005). This suggests that the icy layer is in equilibrium with the current

383 climatology.

384   In the case of the Northern hemisphere, the transition between low and high

385 reflectivity terrains is generally shifted equatorward compared to the ground-ice limit

386 detected by GRS and shows some longitudinal variations (figure 8). Most of this

387 longitudinal variability is likely related to spatial variations of the terrains' physical

388 properties and not to distribution of water ice. Particularly high dielectric values

389   observed at high latitudes in the north Tharsis region are likely caused by a higher

390   density of the near-surface materials. Excluding these regions, the MARSIS ground-

391   ice limit appears shifted equatorward by 6-7° compared to the GRS ground-ice limit.

392   Recent evidences for the presence of ground ice at latitude as low as 43°N have been

393   reported in Arcadia Planitia. Young craters were found to have excavated bright

394   materials with the diagnostic spectral features of water-ice (Byrne et al., 2009). The

395   location of these craters is consistent with the MARSIS limit of ground-ice

396   occurrence. The bright ice deposits excavated by these young craters as well as the

397   ground ice sampled by the Phoenix Lander both point to the presence of layers of

398   nearly pure ice below the regolith.

399   Preliminary MARSIS estimates of ice fraction for the Northern latitudes (50 –

400   100 % by volume, see section 3.3) would also imply the presence of water ice in

401   excess of the regolith porosity. In the Southern hemisphere, estimated values do not

402   allow us to firmly constrain the origin of ground ice. Such a mode of occurrence is

403   inconsistent with pore-filling ice emplaced by direct condensation from atmospheric

404   water vapor. It requires the deposition of an ice-rich material on the surface, such as

405   frost or snow, then buried under a layer of dry regolith formed either by sublimation

406   of dusty ice or by wind transport. Morphologic evidences support this interpretation

407   for both Northern and Southern ground-ice (Head et al., 2003). Repeated freeze thaw

408   (due to long-term variations in obliquity) of an initially ice-saturated regolith can also

409   result in the migration of thin films of adsorbed water along mineral grain surfaces in

410   response to the presence of a temperature gradient. On Earth, this process can result in

411   the formation of massive ice deposits/lenses (Washburn 1980; Williams and Smith

412   1989), which could also explain the Phoenix and GRS observations. However, this

413   mechanism is unlikely to explain ice concentrations of 50-100% to depth >60 m into

414   the subsurface. Beyond the in situ enrichment of ice by repeated freeze/thaw (or the

415   deposition of massive mantles of ice) in response to obliquity variations, there is also

416   the potential survival of water discharged by the outflow channels (Carr 1990) – or

417   the survival of frozen relic of an early ocean (Clifford and Parker, 2001).

418

3.3 Estimation of the volume of water-ice seen by MARSIS

419

420

421   The aim of this paragraph is to propose a rough first order estimate of the

422   water-ice content of the ground based on reflectivity values measured by MARSIS in

423   a simple and ideal case. The accurate inversion of reflectivity values in terms of

424   ground ice content is indeed a challenging task that requires a complete physical

425   modeling of the radar waves reflection process and the knowledge of various

426   properties of the ground. If some of these properties remain unconstrained (layering,

427   density…), it is likely that different models of subsurface composition and structure

428   can lead to similar values of reflectivity, i.e. the inversion process does not lead to a

429   unique solution. Our future work on the retrieval of subsurface composition and

430   texture from MARSIS absolute reflectivity values, based on physical modeling, will

431   be focused on these issues but is beyond the scope of this first study. Here, we

432   calculate the order of magnitude of the amount of water ice required in the subsurface

433   to account for the values of reflectivity measured by MARSIS assuming a

434   homogeneous composition at the scale of a MARSIS resolution cell and fixed

435   parameters for the texture of the ground. By doing that, we aim to provide to the

436   reader an idea of the quantity of ice that can be probed by our method and set a

437   starting point for future studies that will refine the rough value estimated here. In the

438   framework of the simple investigated hypothesis, two values have to be estimated to

439   calculate the quantity of water ice: the thickness of the layer probed by the reflection

440   of the electromagnetic waves on the surface and the ice/rock ratio in this

441   homogeneous layer.

442

443   **3.3.1 Thickness of the probed layer**

444

445   The reflectivity coefficient we determine is related to the permittivity of the

446   surface materials. If one supposes that the subsurface is an infinite homogenous half-

447   space, MARSIS is directly probing the specular reflection of the radar wave. The

448   depth involved in the reflection process is thus given by the skin effect. The loss is

449   given by:

450    $\alpha = 0.091 f \sqrt{\varepsilon} \tan(\delta)$

451   Where f is the frequency (in MHz) and $\tan(\delta)$ the loss tangent.

452   From the value of α one might calculate the skin depth by using:

453    $d = \dfrac{10 \log_{10} e}{\alpha}$

454   Loss tangent for Mars surface rocky materials are expected to vary between 0.004 and

455   0.03 (Picardi et al., 2004) at 5 MHz and were measured to be within the 0.01-0.03

456   range (at 20 MHz) for lava flows west of Ascraeus Mons (Carter et al., 2009). Using

457   0.004 and 0.03 as likely extreme values for the loss tangent, we find the

458   corresponding values for the skin depth to be 780 and 100 m respectively.

459   The MARSIS radar signal has a temporal resolution of $\Delta t = 1$ µs that is equivalent to

460   a propagation length in the media of $2L = c \Delta t / \sqrt{\varepsilon}$ Because this distance is smaller

461   than the skin thickness d, the probed depth in the surface echo is controlled by the

462   temporal resolution. For $\varepsilon = 6$ and 3, this resolution is of 60 to 80 m respectively. It is

463   important to note that this probed thickness is considerably larger than for other usual

464   remote-sensing methods like visible-NIR imaging and spectroscopy (a few µm) or

465   neutrons and gamma-ray spectroscopy (a few tens of cm).

466

467   **3.3.2 Ice/rock ratio**

468

469   In the simple case of a two components mixture examined here, mixing ratios

470   between rock and ice can be roughly estimated using the Maxwell-Garnet rules

471   (Maxwel Garnett, 1904). Maxwell-Garnett rules assume an asymmetric binary

472   mixture with a matrix or environment of dielectric constant: ε_e and spherical

473   inclusions of dielectric constant: ε_i. The medium is assumed to be isotropic. Let f be

474   the volumetric fraction of inclusions in the mixture. The Maxwell-Garnet mixing

475   formula allows us to calculate the effective dielectric constant, ε_{eff}, of the binary

476   mixture:

477
$$\varepsilon_{eff} = \varepsilon_e + 3f\varepsilon_e \frac{\varepsilon_i - \varepsilon_e}{\varepsilon_i + 2\varepsilon_e - f(\varepsilon_i - \varepsilon_e)} \ (10)$$

478   The inversion of dielectric constant value measured by MARSIS in terms of

479   ice / rock ratio requires the knowledge of the dielectric constants of the pure end-

480   members. If the value of $\varepsilon' = 3.1$ for pure water ice at MARSIS wavelength is

481   commonly accepted (Petrenko, 1999) and is not likely to be subject to strong spatial

482   or temporal variations, the choice of a value for the rocky component of the mixture is

483   more problematic. Usually the dielectric constants for volcanic rocky materials are

484   comprised between 6 and 11 (Campbell and Ulrichs, 1969). The mean value found in

485   tropical regions by MARSIS is 6.5. Thus, we assume that the dielectric constant of the

486   dry rock chosen for our calculations are the same as the one measured by MARSIS in

487   equatorial regions. The chosen value is relatively low and even if the nature of the soil

488   changes in certain regions, we can give a lower estimate of the ice / rock mixing ratio.

489   We obtain values of the ice / rock volume mixing ratio of the order of 50 % in the

490   Southern and between 50 and 100 % in the Northern. Although the variability is high,

491   it appears that the average amount of ice present in the subsurface is higher in the

492   Northern hemisphere that in the Southern hemisphere. Furthermore, other

493   observations point to systematic differences between the two hemispheres (see section

494   3.3).

495   The total amount of water stored in the two Martian polar layered terrains

496   (Plaut et al., 2007, Smith et al., 2001) is estimated to be 2.8 10^6 km^3. The atmosphere

497   contains the equivalent of ~3 km^3 of condensed water (Plaut et al., 2001). The total

498   amount of water contained in the subsurface is certainly the main uncertainty in the

499   current inventory of water on Mars. While neutron spectroscopy permitted an

500   estimation of the amount and extent of ice in the top meter of the regolith, low

501   frequency radar techniques now offer the unique opportunity to probe the regolith and

502   quantify the amount of ice at decameters to kilometers scale. In the framework of the

503   ideal hypothesis of a homogeneous subsurface considered in this paragraph, we can

504   estimate the total amount of ground water ice necessary to explain the low values of

505   reflectivity measured by MARSIS. Considering the measured extent of both Northern

506   and Southern ground-ice, the average ice / rock ratio obtained from inversion of

507   MARSIS dielectric measurements and a probed thickness of 60-80 meters, we

508   estimate the potential lower limit of the total volume of ice currently stored at high

509   latitude in the ground to be ~10^6 km^3, of the order of magnitude of the volume of one

510   of the polar caps. As already mentioned at the beginning of this paragraph, future

511   studies dedicated to the physical modeling of the radar reflection process should now

512   be undertaken to examine the influence of the heterogeneity of the subsurface on the

513   inversion of dielectric values in terms of amount of water ice in the subsurface. The

514   case of meters-thick lenses of pure water ice close to the surface should be

515   investigated in priority as this ground structure has been mentioned to interpret recent

516   datasets, especially in-situ observations by the Phoenix Lander (Smith et al., 2009).

517

518 **3.4 Tropical and equatorial minima**

519

520   Examination of the MARSIS surface dielectric map in the equatorial to

521 tropical regions reveals the occurrence of a nearly continuous low reflectivity belt

522 between -30° and +30° latitude. Extremely low values are reached in the Medussae

523 Fossae area ($\varepsilon \approx 3$) (figure 8 and 10). Other minima are encountered in the areas of

524 Meridiani Planum ($\varepsilon \approx 4$) and from Isidis basin to the highlands south of Elysium

525 Planitia ($\varepsilon = 3.5$). The low values of dielectric constants can have various origins:

526 different composition of rocks, low density of surface material, presence of water ice

527 buried beneath a desiccated regolith… Radar measurements alone do not allow

528 discriminating between these different possibilities. When compared to other datasets,

529 it appears that, as in the polar regions, the best match for the MARSIS reflectivity

530 equatorial pattern is obtained from comparison with the GRS WEH map. Indeed, the

531 low reflectivity regions roughly correspond to regions that were shown to be enriched

532 in hydrogen by the GRS instrument suite, with WEH values up to 12%. The

533 interpretation of high hydrogen enrichments detected by GRS in the top first meter of

534 the regolith is still debated. Different explanations have been proposed, like a high

535 abundance of nominally hydrated minerals (Fialips et al., 2005), an interaction of the

536 regolith with atmospheric water vapor (Feldman et al., 2005), or the presence of

537 transient ground ice (Jakosky et al., 2005).

538   The spatial agreement between the low-reflectivity values on the MARSIS

539 map and the H-enriched areas on the GRS map strongly points toward a water-related

540 explanation. In particular, the Medusae Fossae formation terrains, when sounded by

541 MARSIS (Watters et al., 2007), were found to have a bulk real dielectric constant

542 $\varepsilon = 2.9 \pm 0.4$, in agreement with our near-surface estimate. The authors proposed two

543   hypotheses to explain these low values: low-density volcanic deposits or the presence

544   of ice, deposited during a high-obliquity/high-humidity climatic excursion that is

545   currently sublimating at some depth and hydrating the overlying regolith. Spatial

546   correlation between MARSIS and GRS measurements supports this last hypothesis.

547   Unfortunately, the new MARSIS results do not generally allow arguing in favor or

548   one or another of the hypotheses proposed to explain high WEH values measured by

549   GRS. Indeed, the presence of low density / highly hydrated sedimentary materials,

550   such as the ones observed in-situ by the Opportunity rover in Meridiani Planum

551   (Squyres et al., 2004) could explain the observed low radar reflectivity because of

552   their low dielectric constant (Campbell and Ulrichs, 1969) as well as the presence of

553   ground ice as already discussed for high latitudes regions.

554   If the MARSIS radar map does not allow us to choose unambiguously

555   between the pre-cited mechanisms, its main implication is that anomalous surface

556   hydrogen enrichments detected by GRS correspond to anomalies of dielectric

557   constant, possibly related to the presence of H_2O in an unconstrained state, extending

558   down to at least a few decameters below the surface. This is a new and important

559   constraint on the nature and origin of the equatorial anomalies that should be taken

560   into account in future interpretations of these regions.

561

562

563

564 **Conclusion**

565

566   A global 3-5 MHz dielectric map of the Martian surface is built from two

567 years of measurements by the MARSIS instrument. Using MOLA topographic data,

568 we corrected the effect of kilometer-scale roughness and slopes to retrieve the spatial

569 variations of the dielectric constant of near-surface materials. Many parameters are

570 susceptible to influence the dielectric constant of the top decameters below the surface

571 that are probed by the radar wave reflection process. With the use of complementary

572 datasets, we were able to interpret the geographic variations of radar reflectivity in

573 term of surface geological material. From the comparison of the MARSIS map with

574 the hydrogen abundance map derived from GRS measurements, we show that low

575 dielectric values at latitudes poleward of 50-60° are likely to be due to high amount of

576 water ice in the ground.

577   The thickness probed by the MARSIS surface reflectivity is of the order of a

578 few decameters, resulting in a significant increase of the total quantity of ground ice

579 compared to GRS observations, only representative of the first meter below the

580 surface. Assuming a homogenous composition of the ground at the scale of a

581 MARSIS resolution cell as a simple first-order hypothesis, measured values of

582 dielectric constant lead to a minimum estimate of ice stored in the Martian sub-

583 surface to be of the order $\sim 10^6$ km^3, equivalent to a polar cap. Future studies focused

584 on the physical modeling of the reflection process over more realistic models of the

585 subsurface structure and texture will be necessary to refine this rough estimation.

586   At least in the Northern hemisphere the amount of ice appears to be in excess

587 of porosity. Refined analysis of the frequency dependence of the surface reflectivity,

588 together with laboratory measurements of the dispersion relation of ice-rock mixture

589   might help in confirming this observation that would have strong implication for the

590   mechanism of ground ice emplacement.

591   Puzzling anomalies in hydrogen at equatorial latitudes first revealed by the

592   GRS instrument correspond to low reflectivity areas on the MARSIS map. If low

593   reflectivity alone does not permit to discuss further the origin of the hydrogen

594   anomalies, presence of highly hydrated minerals or shallow buried ice, it tells us that

595   the anomalies identified by GRS in the near subsurface actually extend in depth to the

596   first decameters below the surface.

Acknowledgments

609 **References**

610 Aharonson, O., Zuber, M. T. and Rothman, D. H., 2001. Statistics of Mars'

611 topography from the Mars Orbiter Laser Altimeter: Slopes, correlations, and physical

612 models, *J. Geophys. Res., 106*, 23723-23736, doi: 10.1029/2000JE001403

613 Boynton, W. V, and 24 colleagues, 2002. Distribution of Hydrogen in the Near

614 Surface of Mars: Evidence for Subsurface Ice Deposits, *Science, 297*, 81-85

615 Boynton, W. V., and 27 colleagues, 2007. Concentration of H, Si, Cl, K, Fe, and Th in

616 the low- and mid-latitude regions of Mars. Journal of Geophysical Research-Planets.

617 112, 15.

618 Byrne, S., and 17 colleagues, 2009. Distribution of Mid-latitude Ground Ice on Mars

619 from New Impact Craters, *Science*, 325, 1674-1680.

620 Campbell, M. J., Ulrichs, J., 1969. Electrical properties of rocks and their significance

621 for lunar radar observations, *J. Geophys. Res., 74*, 5867-5881.

622 Campbell, B. A., Shepard, M. K., 2003. Coherent and incoherent components in near-

623 nadir radar scattering: Applications to radar sounding of Mars, *J. Geophys. Res.*,

624 Volume 108, Issue E12, pp. 6-1.

625 Campbell, B. A., Hawke, B R., 2005. Radar mapping of lunar cryptomaria east of

626 Orientale basin, *J. Geophys. Res.*, 110, doi :10.1029/2005JE002425.

627 Carr, M. H., 1990. D/H on Mars - Effects of floods, volcanism, impacts, and polar

628 processes, *Icarus* (ISSN 0019-1035), vol. 87, Sept. 1990, p. 210-227.

629 Carter, L. M., et al., 2009. Dielectric properties of lava flows west of Ascraeus Mons.

630 *Geophysical Research Letters*. 36**,** doi:10.1029/2009GL041234.

631   Clifford, S. M., 1993. A model for the hydrologic and climatic behavior of water on

632   Mars. *J. Geoph. Res.*, 98, 10973.

633   Clifford, S. M.; Parker, T. J., 2001. The Evolution of the Martian Hydrosphere:

634   Implications for the Fate of a Primordial Ocean and the Current State of the Northern

635   Plains, *Icarus*, Volume 154, Issue 1, pp. 40-79.

636   Connerney, J. E. P., Acuña, M., Wasilewski, P. J., Kletetschka, G., Ness, N. F.,

637   Rème, H., Lin, R. P., Mitchell, D. L., 2001. The Global Magnetic Field of Mars and

638   Implications for Crustal Evolution*, Geoph. Res. Let., 28*, 4015-4018, doi:

639   10.1029/2001GL013619.

640   Downs, G. S., Goldstein, R. M., Green, R. R., Morris G. A. and Reichley, P. E. 1973.

641   Martian topography and surface properties as seen by radar: The 1971 opposition.

642   *Icarus*, 18, 8-21.

643   Downs, G. S., Reichley, P. E. and Green, R. R. 1975. Radar measurements of Martian

644   topography and surface properties : The 1971 and 1973 oppositions. *Icarus*, 26, 273-

645   312.

646   Duru, F., Gurnett, D., Averkamp, T., Kirchner, D., Huff, R., Persoon, A., Plaut, J.,

647   Picardi, G., 2006. Magnetically controlled structures in the ionosphere of Mars *J.*

648   *Geophys. Res., 111*, 12204-+, doi: 10.1029/2006JA011975.

649   Espley, J., R., Farrell, W., Brain, V, Morgan, V, Cantor, B., Plaut, V, Acuña, M.,

650   Picardi, G., 2007. Absorption of MARSIS radar signals: Solar energetic particles and

651   the daytime ionosphere*, Geoph. Res. Let., 34*, 9101-+, doi: 10.1029/2006GL028829.

652   Evans, J. V. 1962. Radio echoes studies of the Moon. In *Physics and Astronomy of the*

653   *Moon*, ed. Z. Kopal (Nea York : Academic Press), pp 429-479

654   Evans, J. V. and Pettengill, G. H. 1963. The scattering behavior of the Moon at

655   wavelengths of 3.6, 68, and 784 centimeters. *J. Geophys. Res*. 68, 423-477.

656   Feldman, W. C., and 12 colleagues, 2002. Global Distribution of Neutrons from Mars:

657   Results from Mars Odyssey, *Science, 297*, 75-78

658   Feldman, W. C. and 14 colleagues, 2004. Global distribution of near-surface

659   hydrogen on Mars, *J. Geophys. Res., 109*, 9006-+, doi: 10.1029/2003JE002160.

660   Feldman, W. C., Prettyman, T. H., Maurice, S., Nelli, S., Elphic, R., Funsten, H. O.,

661   Gasnault, O., Lawrence, D. J., Murphy, J. R., Tokar, R. L., and Vaniman, D. T., 2005.

662   Topographic control of hydrogen deposits at low latitudes to midlatitudes of

663   Mars, J. Geophys. Res., 110, doi : 10.1029/2005JE002452.

664   Fialips, C. I., Carey, J. W., Vaniman, D. T., Bish, D. L., Feldman, W. C., and Mellon, M.

665   T., 2005. Hydration state of zeolites, clays, and hydrated salts under present-day

666   martian surface conditions: Can hydrous minerals account for Mars Odyssey

667   observations of near-equatorial water-equivalent hydrogen?, Icarus, 178, 74-83.

668   Fung, A. K., Li, Z., Chen, K. S., 1992. Backscattering from a randomly rough

669   dielectric surface, *IEEE Transactions on Geoscience and Remote Sensing, 30*, 356-

670   369

671   Grima, C., Kofman, W., Mouginot, J., Phillips, R., J., Hérique, A., Biccari, D., Seu,

672   R., Cutigni, M., 2009. North polar deposits of Mars: Extreme purity of the water ice,

673   *Geoph. Res. Let., 36*, 3203-+

674   Gurnett, D., and 10 colleagues, 2005. Radar Soundings of the Ionosphere of Mars

675   *Science, 310*, 1929-1933.

676 Head, J. W., Mustard, J. F., Kreslavsky, M. A., Milliken, R. E., Marchant, D. R.,

677 2003. Recent ice ages on Mars. *Nature*. 426, 797-802.

678 Heggy, E., Paillou, P., Costard, F., Mangold, N., Ruffie, G., Demontoux, F.,

679 Grandjean, G., Malézieux, J. M., 2003. Local geoelectrical models of the Martian

680 subsurface for shallow groundwater detection using sounding radars *J. Geophys. Res.*,

681 *108*, 11-+, doi: 10.1029/2002JE001871.

682 Heggy, E., Clifford, S. M., Younsi, A., Miane, J. L., Carley, R., Morris, R. V., 2007.

683 On the Dielectric Properties of Dust and Ice-Dust Mixtures: Experimental

684 Characterization of the Martian Polar-layered Deposits Analog Materials. *Lunar and*

685 *Planetary Institute Conference Abstracts*, Vol. 38, 2007, pp. 1756.

686 Jakosky, B. M., Mellon, M. T., Varnes, E. S., Feldman, W. C., Boynton, W. V.,

687 Haberle, R. M., 2005. Mars low-latitude neutron distribution: Possible remnant near-

688 surface water ice and a mechanism for its recent emplacement, *Icarus*, 175, 58-67.

689

690 Kreslavsky, M., A., Head, J. W., 2000. Kilometer-scale roughness of Mars: Results

691 from MOLA data analysis, *J. Geophys. Res.,* 105, 26695-26712,

692 doi:10.1029/2000JE001259.

693 Krupenio, N. N., 1977. Map-plot of the dielectric constant and density of Martian

694 surface soil, *Kosmicheskie Issledovaniia*, 15, 470-474.

695 Leblanc, F., and 14 colleagues, 2008. Observations of aurorae by SPICAM ultraviolet

696 spectrograph on board Mars Express: Simultaneous ASPERA-3 and MARSIS

697 measurements, *J. Geophys. Res., 113*, 8311-+, doi: 10.1029/2008JA013033.

698 Mangold, N., 2005. High latitude patterned grounds on Mars: Classification,

699   distribution and climatic control. *Icarus*. 174, 336-359.

700   Maxwell Garnett, J. C., 1904. Colours in metal glasses and metal films. *Transaction*

701   *of the Royal Society of London* **CCIII**, 481-502.

702   Mellon, M., Jakosky, B. M., 1993. Geographic variations in the thermal and diffusive

703   stability of ground ice on Mars. *Journal of Geophysical Research*. 98, 3345-3364.

704   Mellon, M. T., Feldman, W. C., Prettyman, T. H., 2004. The presence and stability of

705   ground ice in the southern hemisphere of Mars. *Icarus*. 169, 324-340.

706   Mellon, M. T., Arvidson, R. E., Marlow, J. J., Phillips, R. J., Asphaug, E., 2008.

707   Periglacial landforms at the Phoenix landing site and the northern plains of Mars.

708   *Journal of Geophysical Research-Planets*. 113.

709   Mitrofanov, I., and 11 colleagues, 2002. Maps of Subsurface Hydrogen from the High

710   Energy Neutron Detector, Mars Odyssey, *Science, 297*, 78-81.

711   Mouginot, J., Kofman, W., Safaeinili, A., Herique, A., 2008. Correction of the

712   ionospheric distortion on the MARSIS surface sounding echoes*, Plan. and Space Sci.,*

713   *56*, 917-926

714   Mouginot, J., Kofman, W., Safaeinili, A., Grima, C., Herique, A., Plaut, J.~J. 2009.

715   MARSIS surface reflectivity of the south residual cap of Mars, *Icarus* 201, 454-459

716   Niles, P. B., Michalski, J., 2009. Meridiani Planum sediments on Mars formed

717   through weathering in massive ice deposits. *Nature Geoscience*. 2, 215-220.

718   Neumann, G. A.; Abshire, J. B.; Aharonson, O.; Garvin, J. B.; Sun, X.; Zuber, M. T.,

719   2003. Mars Orbiter Laser Altimeter pulse width measurements and footprint-scale

720   roughness, *Geophysical Research Letters*, Volume 30, Issue 11, pp. 15-1.

721 Nouvel, J. F., 2002. Sondage du sous-sol martien par un radar basse-fréquence depuis

722 un satellite en orbite basse: analyses physiques et préparation des données, PhD

723 Thesis, *Université Joseph Fourier, Grenoble.*

724 Nouvel, J., F., Herique, A., Kofman, W., Safaeinili, A., 2004. Radar signal

725 simulation: Surface modeling with the Facet Method, *Radio Sci., 39*, RS1013

726 Petrenko, V. F., Whitworth, R. W., 1999. *Physics of Ice*. Oxford Univ. Press, New

727 York.

728 Pettengill, G. H., Shapiro, I. I., and Rogers, A. E. E. 1973. Topography and radar

729 scattering properties of Mars. Icarus, 18, 22-28.

730 Picardi, G., and 12 colleagues, 2004. Performance and surface scattering models for

731 the Mars Advanced Radar for Subsurface and Ionosphere Sounding (MARSIS).

732 Planetary and Space Science. 52, 149-156.

733 Picardi, G., and 33 colleagues, 2005. Radar Soundings of the Subsurface of Mars,

734 *Science, 310*, 1925-1928.

735 Plaut, J., J., and 23 colleagues, 2007. Subsurface Radar Sounding of the South Polar

736 Layered Deposits of Mars, *Science, 316*, 92-95.

737 Safaeinili, A., Kofman, W., Nouvel, J. F., Herique, A., Jordan, R., 2003.

738 Impact of Mars ionosphere on orbital radar sounder operation and data processing,

739 *Plan. and Space Sci., 51*, 505-515.

740 Safaeinili, A., Kofman, W., Mouginot, J., Gim, V, Herique, A., Ivanov, A., Plaut, J.,

741 Picardi, G., 2007. Estimation of the total electron content of the Martian ionosphere

742 using radar sounder surface echoes, *Geoph. Res. Let., 34*, 23204-+,

743   doi:10.1029/2007GL032154.

744   Schorghofer, N., Aharonson, O., 2005. Stability and exchange of subsurface ice on

745   Mars. Journal of Geophysical Research-Planets. 110, 16.

746   Seu, R., and 11 colleagues, 2007. SHARAD sounding radar on the Mars

747   Reconnaissance Orbiter, J. Geophys. Res., 112, doi :10.1029/2006JE002745.

748   Sihvola, A., 1999. *Electromagnetic mixing formulas and applications*. IEEE.

749   Simpson, R. A., Tyler, G. L., Brenkle, J. P. and Sue, M. 1979. Viking bistatic radar

750   observations of the Hellas Basin on Mars: Preliminary results, *Science*, 203, 153-173.

751   Simpson, R. A., Tyler, G. L. Harmon, J. K. and Peterfreund, A. R. 1982. Radar

752   measurement of small-scale surface texture : Syrtis Major, *Icarus*, 49, 258-283.

753   Simpson, R. A, Harmon, J. K, Zisk, S. H, Thompson, T.~W. and Muhleman, D. O.

754   1992. Radar determination of Mars surface properties in *Mars*, The university of

755   Arizona Press, p. 652-685.

756   Smith, D. E., and 23 colleagues, 2001. Mars Orbiter Laser Altimeter: Experiment

757   summary after the first year of global mapping of Mars, *J. Geophys. Res., 106*, 23689-

758   23722, doi:10.1029/2000JE001364.

759   Smith, M. D., 2004. Interannual variability in TES atmospheric observations of Mars

760   during 1999-2003. Icarus. 167, 148-165.

761   Smith, P. H., and 35 colleagues, 2009. H_2O at the Phoenix landing site. Science, 325,

762   58-61.

763   Squyres, S. W., Clifford, S. M., Kuzmin, R. O., Zimbelman, J. R., Costard, F. M.,

764   1992. Ice in the Martian Regolith. In: H. H. Kieffer, (Ed.), Mars. The University of

765   Arizona Press.

766   Squyres, S. W., and 18 colleagues, 2004. In Situ Evidence for an Ancient Aqueous

767   Environment at Meridiani Planum, Mars. Science. 306, 1709-1714.

768   Ulaby, F., Moore, T. R., Fung, A., 1986. Microwave Remote Sensing, Artech House

769   Publishers.

770   Washburn, A. L., 1980. Permafrost features as evidence of climatic change, *Earth*

771   *Science Reviews*, Volume 15, Issue 4, p. 327-402.

772   Watters, T. R., and 12 colleagues, 2007. Radar Sounding of the Medusae Fossae

773   Formation Mars: Equatorial Ice or Dry, Low-Density Deposits?, *Science,* 2007*, 318*,

774   1025.

775   Williams P. J., Smith M. W., 1989. The Frozen Earth: Fundamentals of Geocryology,

776   Cambridge University Press, , Cambridge (1989). ISBN 0 521 365334 1.

777

778
779

780

781

782

783 **Figure Captions**

784

785 **Figure 1:** Top: a typical MARSIS pulse measured over the South Polar Layered

786 Deposits (orbit #2682, pulse 718) in dB. The surface echo is recorded at about t = 130

787 µs after the opening of the receiver's window. Another strong echo, attributed to the

788 reflection on the bedrock below this ice, is received at t = 170 µs. Bottom: the criteria

789 C as defined in equation 1 calculated for the same MARSIS pulse. The position of the

790 surface echo is indisputably highlighted by the high value of C,

791 **Figure 2.** Top to bottom: the radargram of orbit #2787, the position of the surface

792 echo detected by our algorithm, the power reflected by the surface in dB.

793 **Figure 3** (a) Left: raw reflectivity as function of the Solar Zenith Angle (SZA). (b)

794 Right: mean reflectivity as function of the Total Electron Content. Both graphics have

795 been plotted using the entire set of data at 4 MHz.

796 **Figure 4.** Reflectivity corrected for absorption as function of the total electron

797 content. The graph has been plotted using the entire set of data at 4 MHz.

798 **Figure 5. A:** Reflectivity map at 3-5 MHz of the Martian surface as seen by

799 MARSIS. Red corresponds to high reflectivity and blue to low reflectivity. Grey

800 regions correspond to a lack of data. The map is in cylindrical projection. The spatial

801 resolution is 0.5 bin per degree.

802 **B:** Reflectivity map based on simulated radargrams. Grey regions correspond to a

803 lack of data. The map is a cylindrical projection. The resolution is 0.5 bin per degree.

804 **C:** Roughness map from Kreslavsky and Head (2000)

805   **Figure 6.** The image on the left has been provided by HIRISE on board MRO

806   (PSP_001736_2605, credit: NASA/JPL/University of Arizona). This image with 25

807   cm resolution per pixel shows in detail the dunes in Olympia Undae. The radargram

808   on top corresponds to a part of orbit #3674 of MARSIS/MEX over this region. The

809   bottom image is the MOLA topography corresponding to the MARSIS track.

810   **Figure 7.** Reflectivity map corrected for roughness effect. As described in the text,

811   the reflectivity has been calibrated using a reference making it possible to provide the

812   corresponding dielectric constant. The map is a cylindrical projection. The spatial

813   resolution is one bin per degree. Grey background corresponds either to a lack of data

814   or a removal of data corrupted by artefacts (effects of magnetic field, high surface

815   roughness).

816   **Figure 8**: (A) MARSIS dielectric map. Same as figure 7.

817   (B) Global interpolation of the dielectric map (A) using 8-order

818   spherical harmonics adjustment.

819   (C) Global map of hydrogen concentration in the top meter of the

820   regolith obtained by the neutrons spectrometer of the GRS / Mars

821   Odyssey instruments suite (data from Feldman et al., 2004).

822   Concentration is expressed as Water Equivalent Hydrogen

823   abundance in weight percent.

824   All maps are gridded in Robinson projection.

825   **Figure 9:** Longitudinal averages of MARSIS surface real dielectric constant and GRS

826   neutrons spectrometer WEH concentration. Red crosses correspond to the dielectric

827   constant values measured by MARSIS and plotted on figure 8.A whereas the red

828   curve corresponds to the interpolated MARSIS map (figure 8.B). WEH values are

829   calculated from the map plotted in figure 8.C.

830   **Figure 10**: A: Visible color map (Viking), B: Thermal inertia map (TES), C:

831   MARSIS reflectivity map. The comparison between these maps shows that the limits

832   displayed on the MARSIS reflectivity map do not correspond to systematic changes

833   of albedo and thermal inertia, indicating that the surface material remains unchanged

834   while subsurface material is different.

835 **Tables**

Central Frequency	3 MHz	4 MHz	5 MHz
Total electron Content ($10^{15}m^{-2}$)	3	7.5	7.5
Solar Zenith Angle	85°	70°	60°

836

837 **Table 1**. Summary of the limits used to select the data. Measurements are kept when

838 the total electron content is below the limit indicated by the first line and when the

839 solar zenith angles are above the limit indicated by the second line.

840
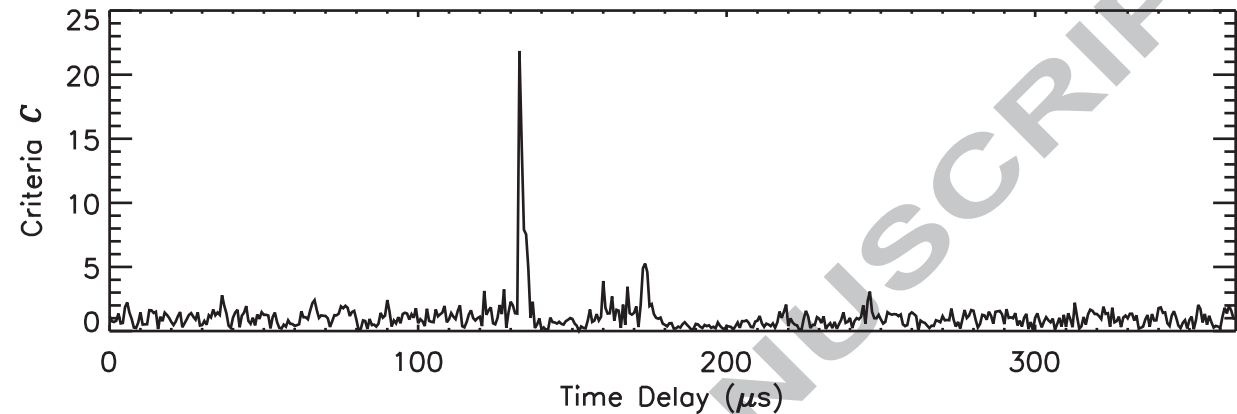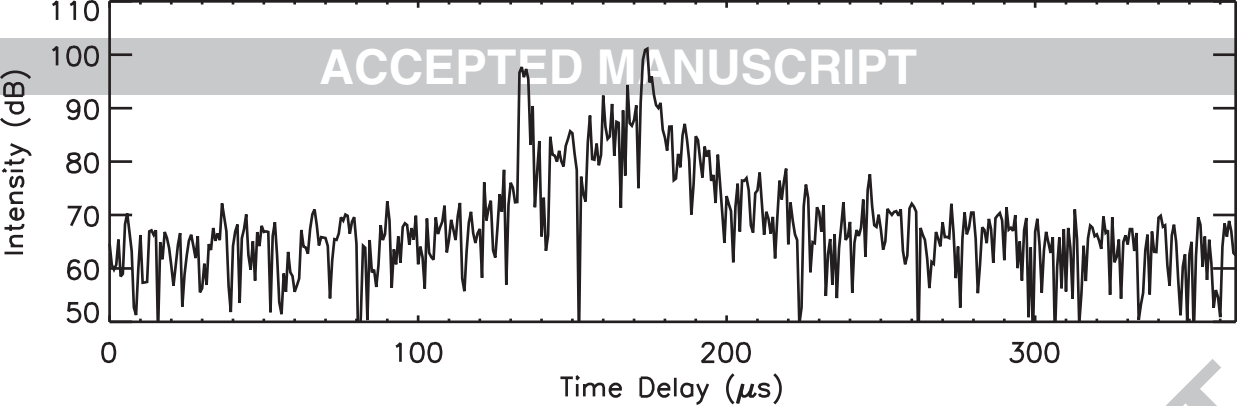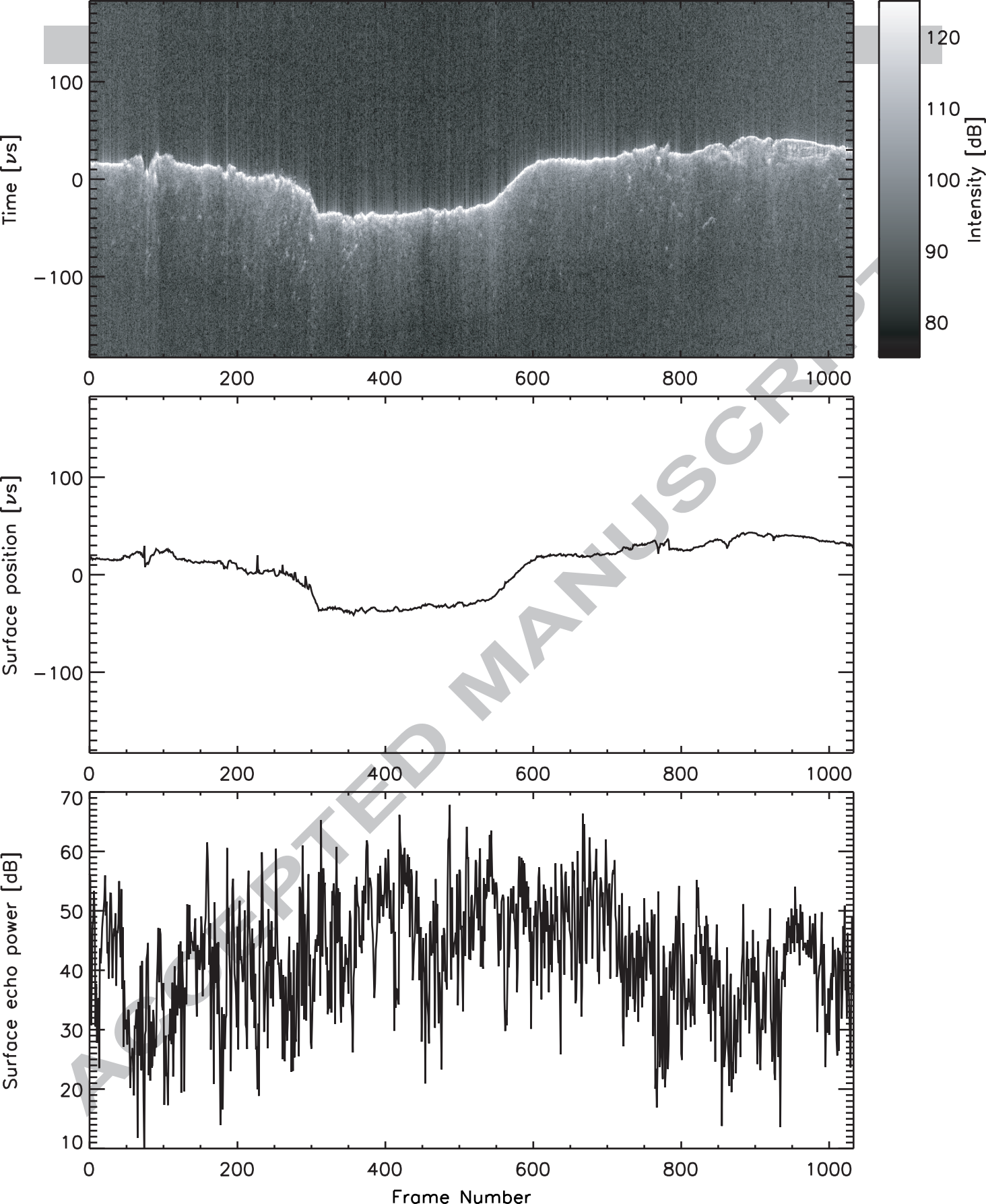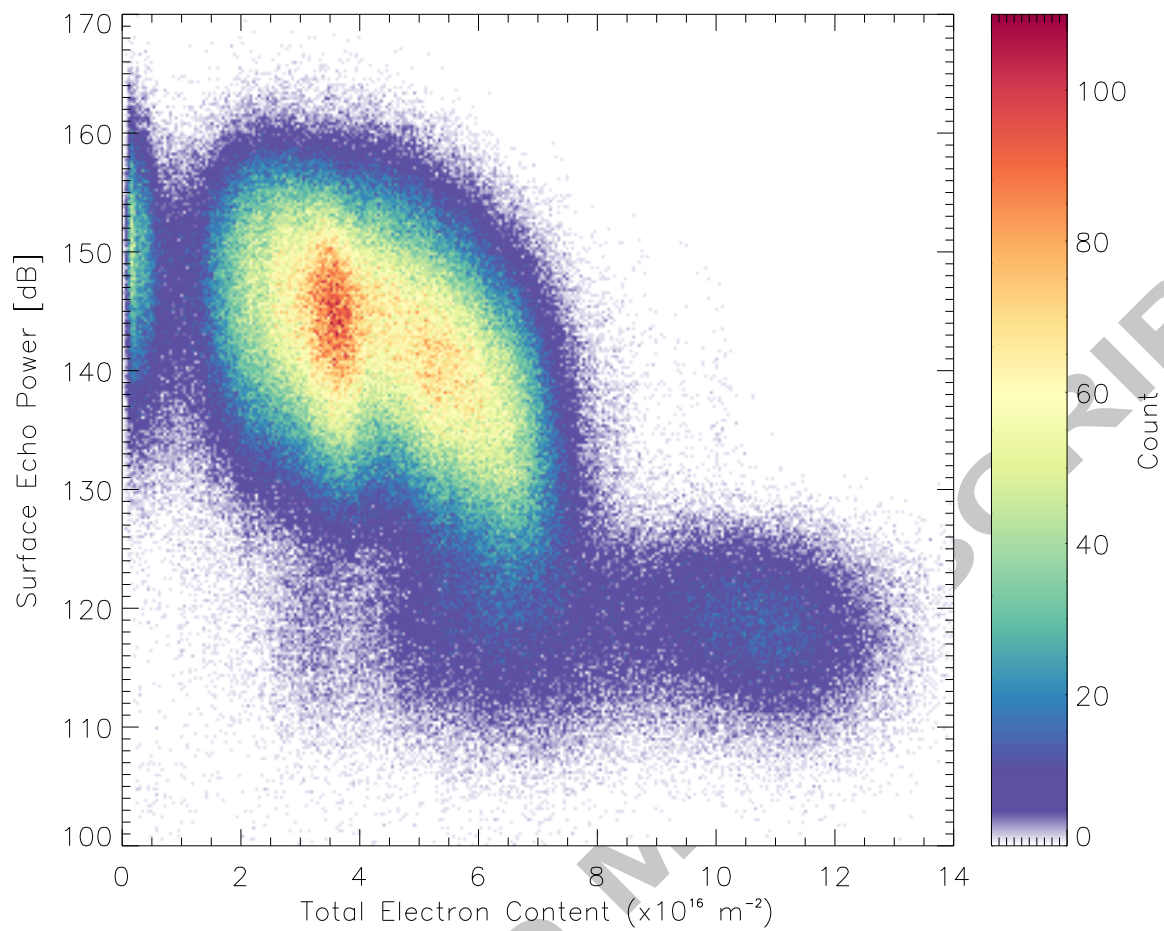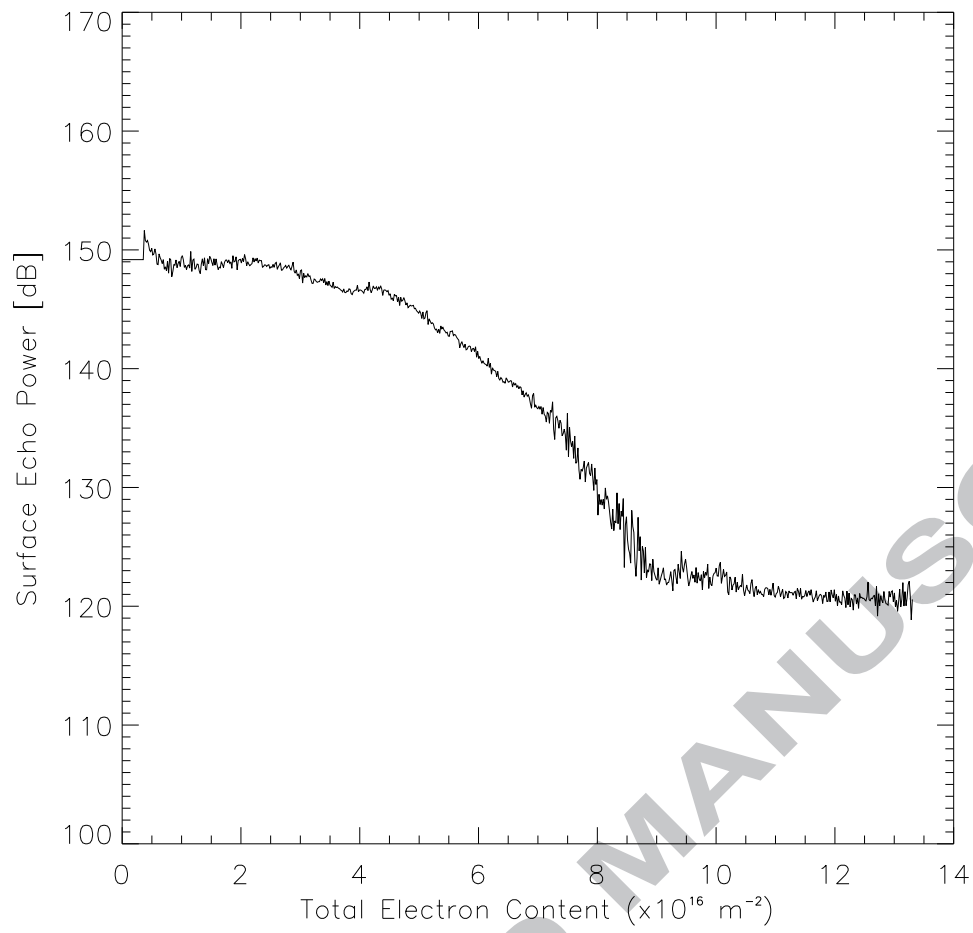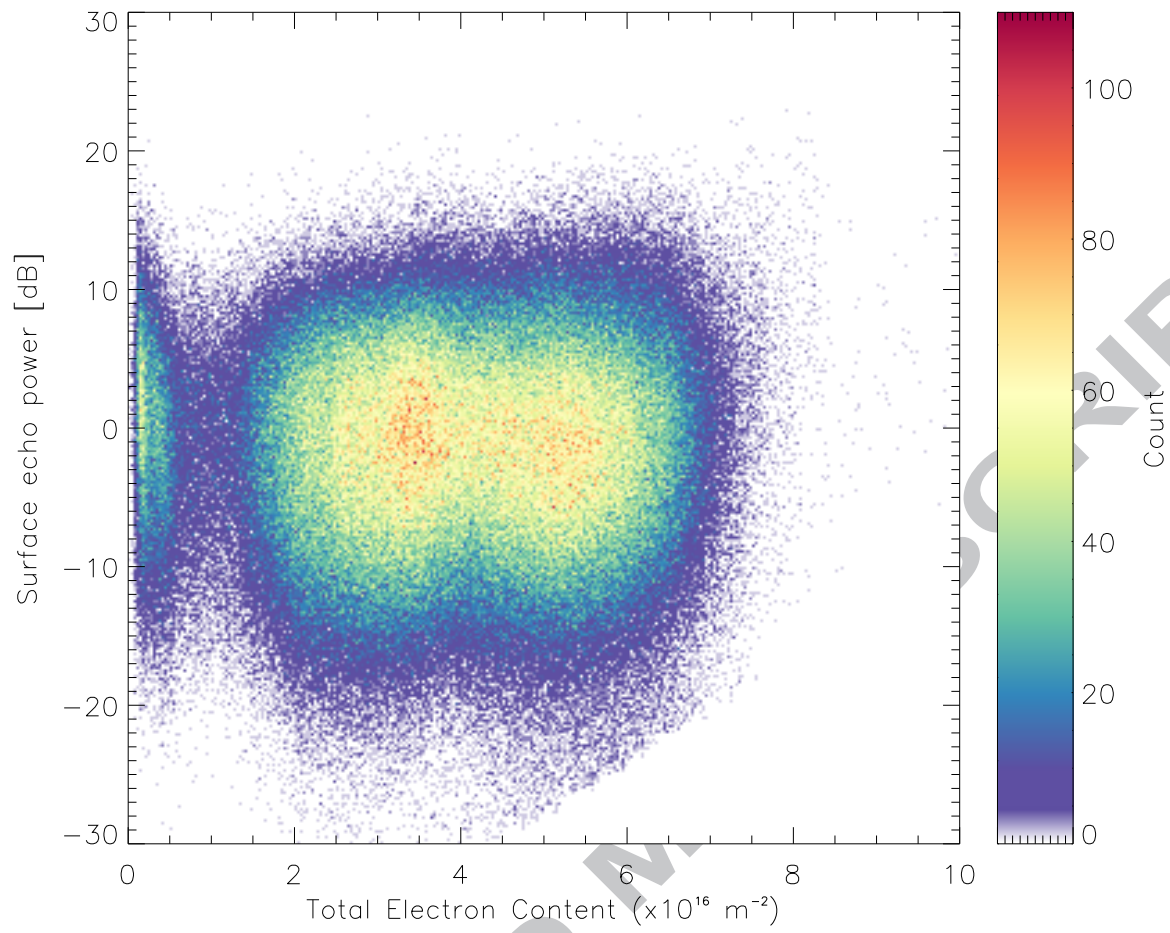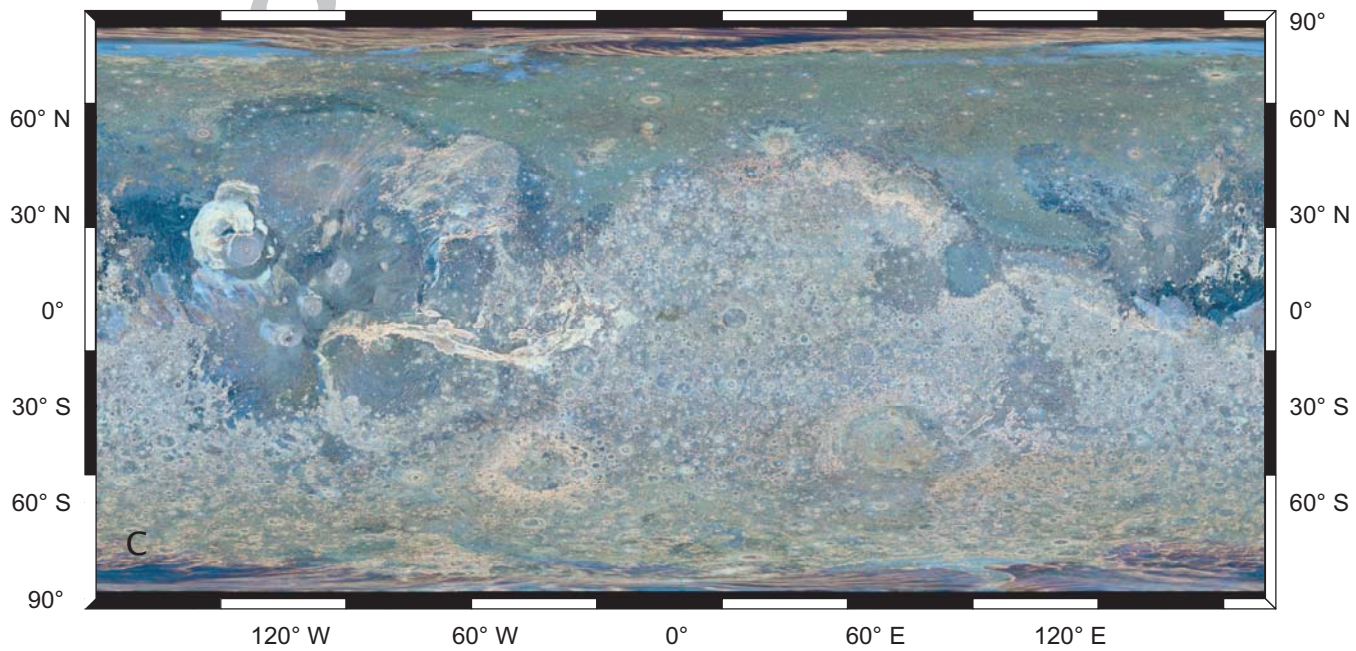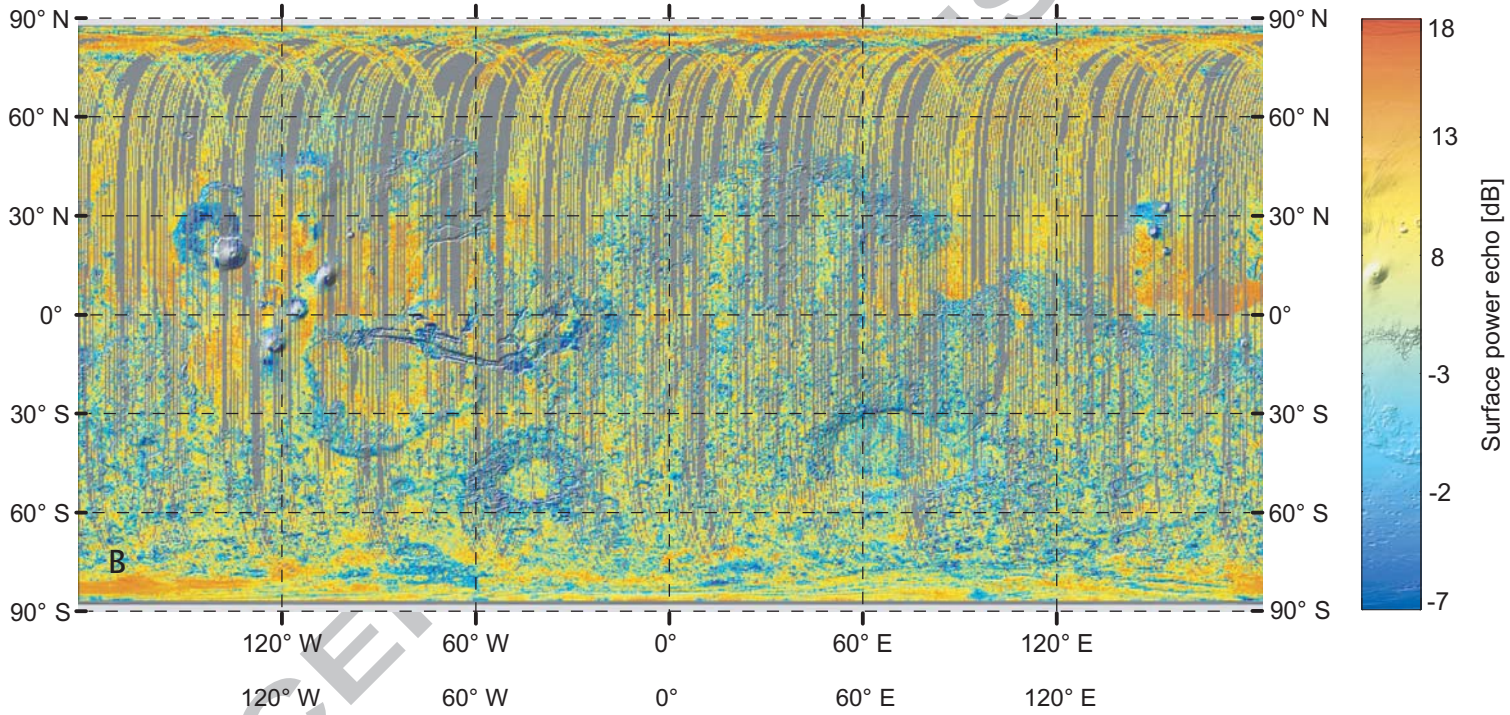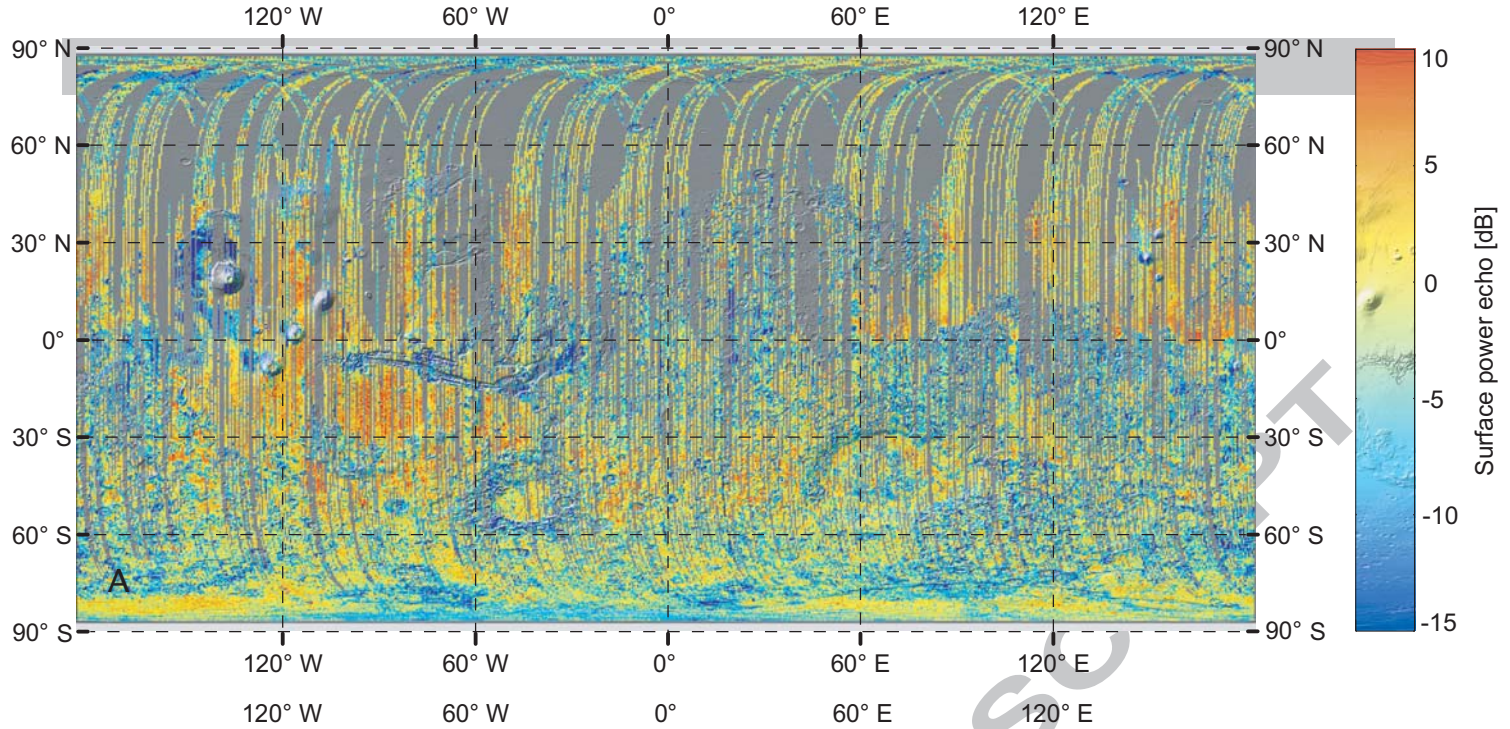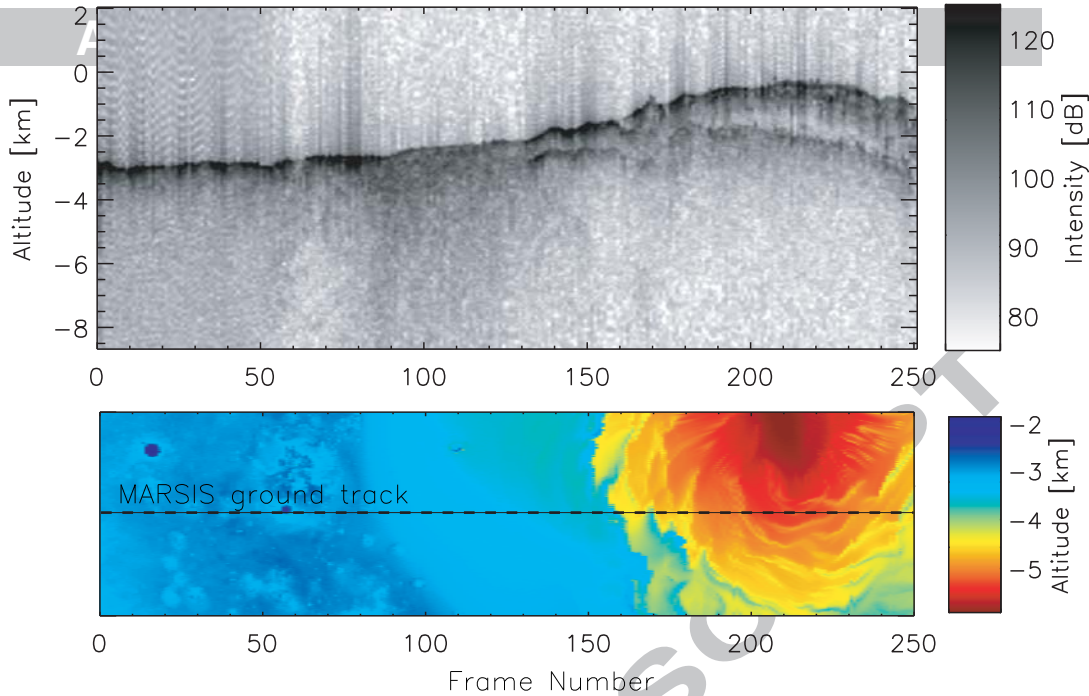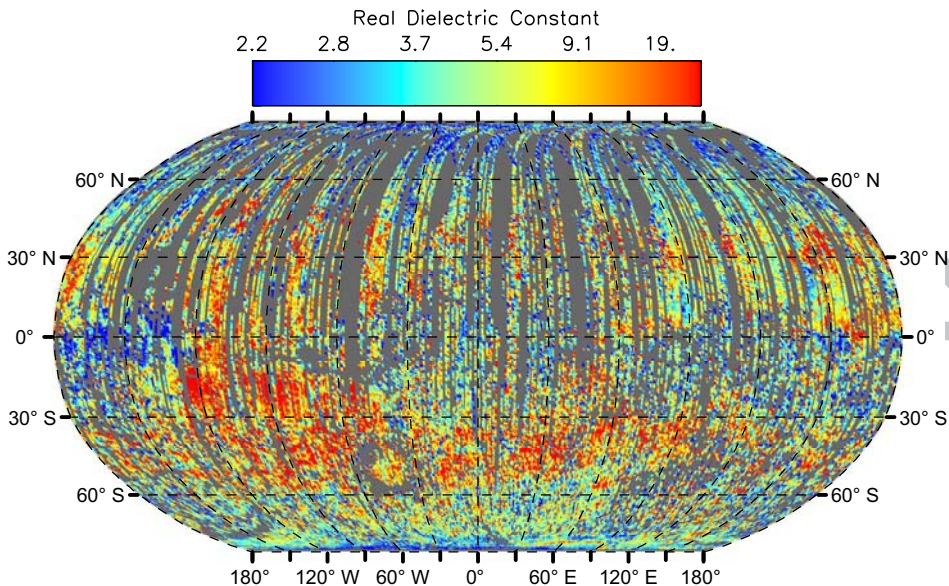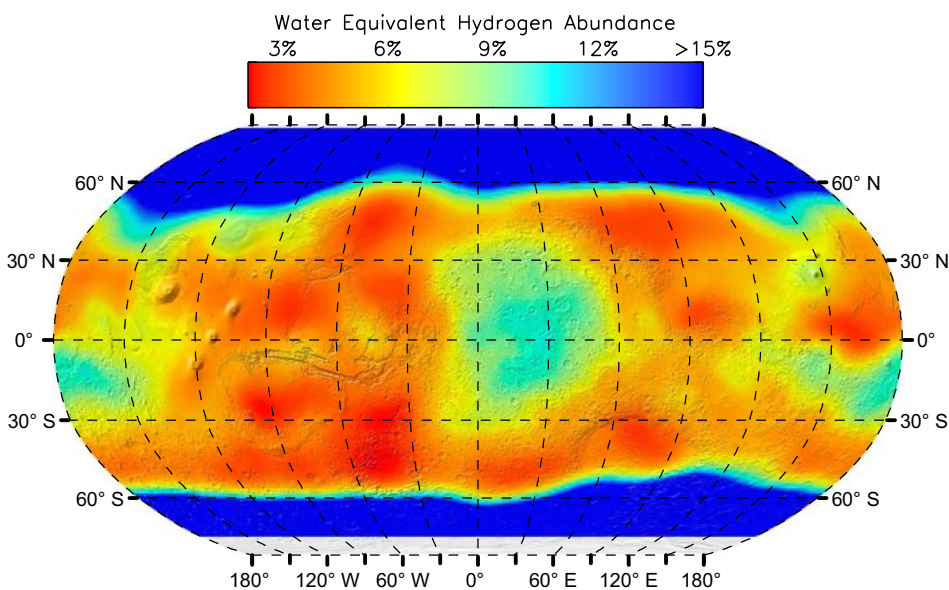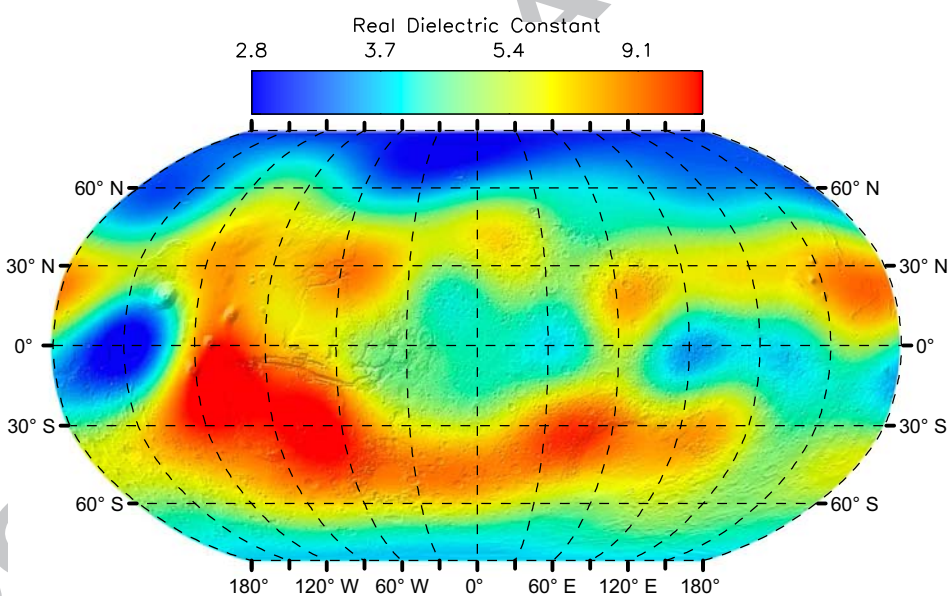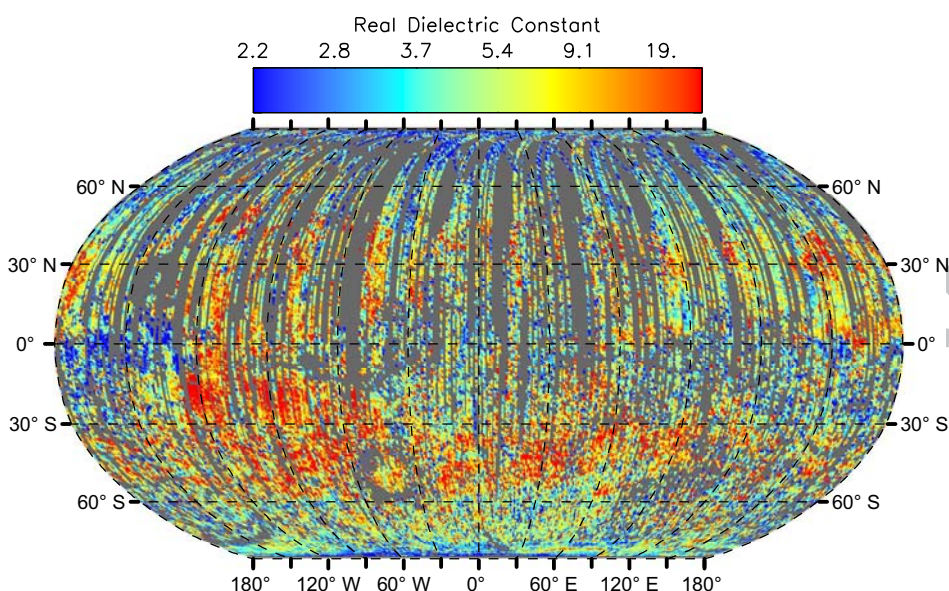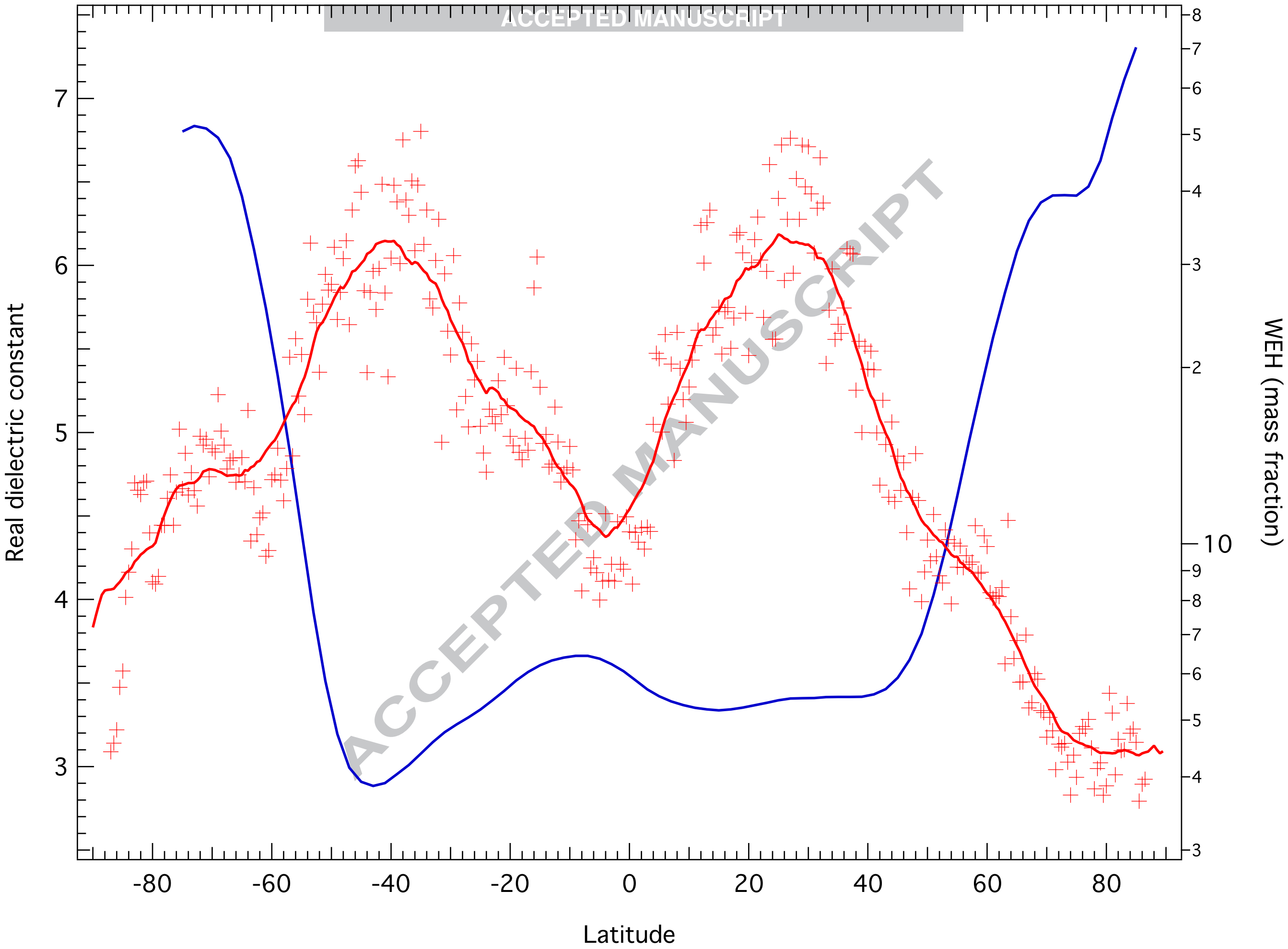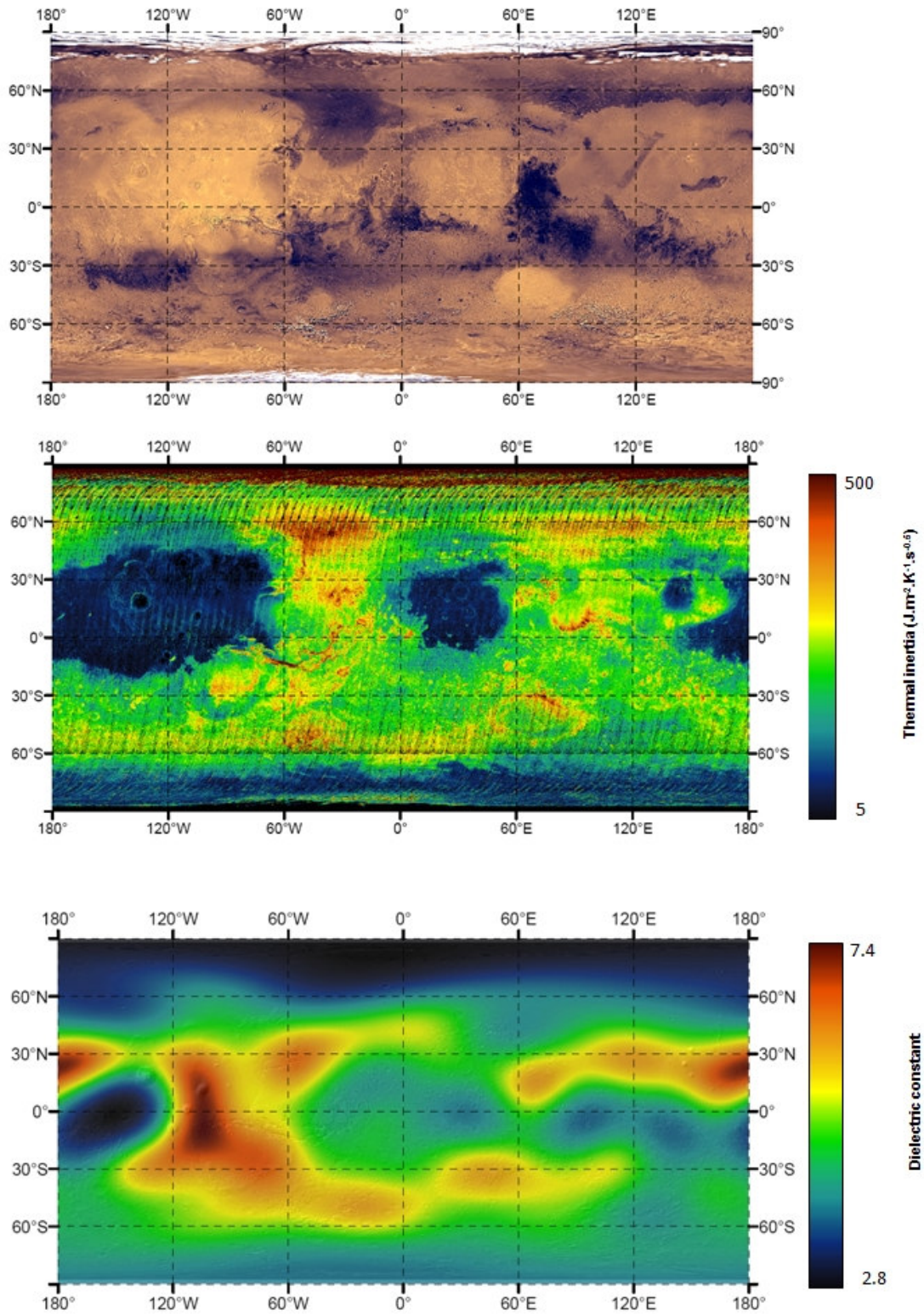
A

B

C

3674

MARSIS ground track

Real Dielectric Constant

2.2   2.8   3.7   5.4   9.1   19.

Real Dielectric Constant

2.8   3.7   5.4   9.1

Water Equivalent Hydrogen Abundance

3%   6%   9%   12%   >15%

Corresponding Author: Dr. Jeremie Mouginot, Ph.D.

Corresponding Author's Institution: University of California

First Author: Jeremie Mouginot, Doctor

Order of Authors: Jeremie Mouginot, Doctor; Antoine Pommerol; Wlodek Kofman; Pierre Beck; Bernard Schmitt; Cyril Grima; Alain Herique; Ali Safaeinili; Jeffrey J Plaut

Abstract: We extracted the surface echo power from two years of MARSIS measurements. The retrieved values are calibrated to compensate for changes in the distance of the spacecraft to the surface and for the attenuation of the signal by the ionosphere. The results are used to build the first global map of surface echo power at 3-5 MHz. The surface echo power variations are primarily caused by km-scale surface roughness. Then, we derive the values of dielectric constant of the shallow subsurface materials by normalizing the surface echo power map using a simulation of MARSIS signal from the MOLA topography. As a result, we obtain a map that characterizes the dielectric properties of the materials down to a few decameters below the surface. Dielectric properties vary with latitude, with high values in mid-latitudes belts (20-40°) and lower values at both equatorial and high latitudes. From the comparison of MARSIS reflectivity map to GRS observations, we conclude that the reflectivity decrease observed poleward of 50-60° corresponds to the onset of water-ice occurrence within the regolith. Assuming homogenous ground composition and texture at the scale of the MARSIS resolution cell, our inferred volume of ground water ice is of 106 km3, equivalent to a polar cap. Low reflectivity areas are also observed in equatorial regions. From radar studies alone, equatorial low dielectric constant values could have different interpretations but the correlation with GRS hydrogen distribution rather points toward a water related explanation.